Geochemistry, Geophysics, Geosystems®

AGU ADVANCING EARTH AND SPACE SCIENCES

RESEARCH ARTICLE
10.1029/2024GC012048

Continuous Subsidence of Dallol Volcano Caused by Magmatic, Hydrothermal, and Salt Dissolution Processes: Insights From InSAR Observations

Birhan A. Kebede[1,2], Carolina Pagli[2], Derek Keir[1,3], Freysteinn Sigmundsson[4], Alessandro La Rosa[2], Hua Wang[5], Elias Lewi[6], and Snorri Gudbrandsson[7]

[1]Department of Earth Sciences, University of Florence, Florence, Italy, [2]Department of Earth Sciences, University of Pisa, Pisa, Italy, [3]School of Ocean and Earth Science, University of Southampton, Southampton, UK, [4]Nordic Volcanological Center, Institute of Earth Sciences, University of Iceland, Reykjavik, Iceland, [5]Guangdong Provincial Key Laboratory for Land Use and Consolidation, College of Natural Resources and Environment, South China Agricultural University, Guangzhou, China, [6]Institute of Geophysics, Space Science and Astronomy, Addis Ababa University, Addis Ababa, Ethiopia, [7]Energy Sector Management Assistance Program (ESMAP), The World Bank, Washington, DC, USA

Key Points:

- InSAR study of deformation in the magmatically and geothermally active area of Dallol, Danakil, East African rift
- InSAR time series and velocity maps show three subsiding deformation signals on the Dallol volcano and its surroundings
- InSAR modeling indicates that the subsidence signals are related to active magmatism, hydrothermal and salt dissolution processes

Supporting Information:

Supporting Information may be found in the online version of this article.

Correspondence to:

B. A. Kebede and D. Keir,
birhan.kebede@unifi.it;
derekboswell.keir@unifi.it

Citation:

Kebede, B. A., Pagli, C., Keir, D., Sigmundsson, F., La Rosa, A., Wang, H., et al. (2025). Continuous subsidence of Dallol volcano caused by magmatic, hydrothermal, and salt dissolution processes: Insights from InSAR observations. *Geochemistry, Geophysics, Geosystems*, *26*, e2024GC012048. https://doi.org/10.1029/2024GC012048

Received 17 DEC 2024
Accepted 28 FEB 2025

Author Contributions:

Conceptualization: Birhan A. Kebede, Carolina Pagli, Derek Keir, Freysteinn Sigmundsson
Data curation: Carolina Pagli, Derek Keir, Alessandro La Rosa, Elias Lewi
Formal analysis: Birhan A. Kebede
Investigation: Birhan A. Kebede
Methodology: Birhan A. Kebede, Alessandro La Rosa

Abstract The Dallol volcano on the axis of the Erta Ale ridge (Afar rift) offers an ideal opportunity to study the interaction between magmatic and hydrothermal processes. Volcanic activity in Dallol has developed in an area below sea level with a salt plain. Dallol has been actively deforming since InSAR measurements started in the area in 2004. However, the source of deformation under Dallol remains unclear. We present a new InSAR study of Dallol from 2014 to 2023 showing at least three concentric deformation signals of range increase consistent with subsidence with rates ranging 23–43 mm/yr in the satellite Line-of-Sight. The main subsidence occurs at Dallol volcano, and two smaller maxima occur at the Black Mountain and the Bubbling Pool areas to the south and southwest of Dallol, respectively. Our modeling indicates that the deformation is caused by contraction of three sill-shaped sources (Okada tensile dislocations) at depths ranging 0.6–1.5 km, each with a volume contraction in the range 1.8–5.5 × 10^4 m^3/yr. Time series analysis shows that the subsidence at Dallol volcano and Black Mountain was continuous and linear in time. Furthermore, an integrated observation of InSAR with the geology, resistivity image and seismic reflection of the area suggest that the 1.5 km deep source under Dallol is the cooling and contraction of a magma reservoir. At Black Mountain (1 km deep) and Bubbling Pool (0.6 km deep), the data suggest that subsidence is due to either a pressure decreases in the shallow hydrothermal system and/or salt dissolution.

Plain Language Summary Ground motions are common in geologically active regions, such as the East African rift. This can be due to faults, molten rock (magma), or heated water (hydrothermal fluids) moving beneath the Earth's surface and causing it to move. In this study, we investigate the causes of ground motion at Dallol volcano and its surroundings, a spectacular area in the northern Afar rift with distinctive geological and environmental features. In this study, we used a satellite measurement technique called InSAR to map ground motion at Dallol from 2014 to 2023 with sub-cm accuracy. Our study revealed the three areas where the ground is constantly lowering at rates of up to nearly 5 cm per year. These areas are Dallol volcano, Bubbling Pool and Black Mountain. To find out what process below the ground causes the surface to move, we created model simulations of our satellite observations and found that three sheet-shaped areas of decompression exist under Dallol. These simulations combined with other observations of the subsurface suggest that the sources of decompression are diverse: due to magma cooling and contracting, pressure drops in the hydrothermal steam zone, and areas where the subsurface salt is dissolving.

1. Introduction

The East African Rift (EAR) system is a continental rift that hosts several active volcanoes with intense geothermal activity. Many of these volcanoes are rapidly deforming (Albino & Biggs, 2021), but in many cases it is not clear whether the observed deformation is related to magmatic processes or to other sources such as hydrothermal fluid flow (Albino & Biggs, 2021; Kebede et al., 2023). Thus, it is rarely clear how magmatic and hydrothermal systems interact. Understanding the position, behavior, and fluid flow pathways of the coupled magmatic and hydrothermal system is important for evaluating the geothermal potential of the volcanoes, and for monitoring the sites once energy production starts (e.g., Drouin et al., 2017; Receveur et al., 2019).

Project administration: Carolina Pagli, Derek Keir, Freysteinn Sigmundsson
Resources: Carolina Pagli, Derek Keir, Freysteinn Sigmundsson
Software: Alessandro La Rosa, Hua Wang
Supervision: Carolina Pagli, Derek Keir, Freysteinn Sigmundsson
Validation: Carolina Pagli, Derek Keir, Freysteinn Sigmundsson, Alessandro La Rosa, Hua Wang, Elias Lewi
Visualization: Birhan A. Kebede, Alessandro La Rosa, Hua Wang
Writing – original draft: Birhan A. Kebede, Carolina Pagli, Derek Keir, Freysteinn Sigmundsson, Hua Wang
Writing – review & editing: Alessandro La Rosa, Elias Lewi, Snorri Gudbrandsson

Satellite geodetic techniques, such as Interferometric Synthetic Aperture Radar (InSAR), can be used to measure ground motions at volcanoes, and then model the subsurface sources of the deformation. The Dallol volcano is within an isolated and remote region in the Danakil depression of the EAR, and it is one of the currently deforming volcanoes in the EAR where the origin of the ground motions is unclear (Albino & Biggs, 2021; Battaglia et al., 2021). Given that the area is known for diverse salt mineralization and dissolution, this process needs to be taken in to consideration when interpreting ground motion. Thermal destabilization of hydrated minerals by a magmatic intrusion causing hydrolysis at the Dallol area has been interpreted to be responsible for the long-term formation of the Dallol salt dome and crater (e.g., Lopez-García et al., 2020; Otálora et al., 2022), though this was not calibrated with measurements of ground motion. Globally, we are not aware of any prior studies showing salt dissolution as the cause of geodetically measured ground motions.

In this study, we used Sentinel-1A/B SAR data acquired over the years 2014–2023 to study the spatial and temporal pattern of deformation at Dallol in detail. We then use time series analysis and elastic modeling to constrain the geometry, depth and temporal behavior of the sources responsible for the deformation, aiming to improve our understanding of the subsurface magmatic and hydrothermal systems. This analysis allows us to capture the mode of deformation and determine the sources responsible for the observed ground motion signals.

Additionally, to further support our InSAR observations, we supplement our interpretations with the use of geology, and previously acquired geophysical data (magnetic, seismic reflection, electrical resistivity, and gravity) from Dallol.

1.1. Geological Background

The Afar rift, which is in the EAR system, has formed in response to the divergent motions between Arabian, Somalian, and Nubian plates since the Oligocene-Miocene (Rime et al., 2023; Tesfaye et al., 2003). Geodetic GNSS (Global Navigation Satellite System) measurements indicate that the Nubian and Somalian plates are moving apart at a full extension rate of ∼5–7 mm/yr, while the Arabian and the Nubian plates are separating at a rate of ∼15–20 mm/yr (ArRajehi et al., 2010; Birhanu et al., 2016; Doubre et al., 2017; McClusky et al., 2010; Stamps et al., 2021; Viltres et al., 2022). Afar is a topographically depressed area bounded by the Ethiopian Plateau in the west, the Danakil block in the east, and the Somalian plateau in the south (Figure 1a).

In the northern portion of the Afar rift, known as the Danakil depression, the rift floor is at low elevation reaching −125 m below sea level, and is therefore one of the lowest emerging points on Earth. The Danakil depression is a relatively narrow (50–200 km wide), ∼300 km long rift that is NNW-oriented and is filled dominantly by evaporite deposits forming a salt plain. The crustal thickness varies from 25 km in the south to 15 km in the north (e.g., Hammond et al., 2011; Keir et al., 2013; Lewi, 2024; Makris & Ginzburg, 1987). The axial region of the Danakil depression is marked by the NNW-oriented Erta Ale and Tat'Ale magmatic segments, both hosting several volcanoes that are actively deforming (e.g., Barberi & Varet, 1970; Illsley-Kemp et al., 2018; Keir et al., 2013; Moore et al., 2021; Pagli et al., 2012).

Dallol is an active magmatic area situated near the northern end of the Erta Ale magmatic segment within the Danakil depression (e.g., Battaglia et al., 2021; Nobile et al., 2012). It is characterized by geologic formations including deposits of hydrothermal and widespread salt structures (Figures 1c–1i; Figure S1 in Supporting Information S1). The climate is severe with a daily average temperature of 30–50°C (e.g., Cavalazzi et al., 2019), and the interaction between the evaporite deposits and the hydrothermal fluids commonly leads to highly acidic fluid chemistry (Belilla et al., 2019). Dallol volcano is elevated to about 50 m above the surrounding salt plain and has a crater about 1 km in diameter, inferred to have formed by a phreatic eruption without any volcanic deposits (Holwerda & Hutchinson, 1968). The crater is filled mainly by deposits of evaporites, sediments, various salt structures, and has fumaroles, hot springs, small geysers, and hydrothermal minerals (e.g., Franzson et al., 2015; Lopez-García et al., 2020). Apart from the crater area, acidic and non-acidic pools, small size mud craters (Franzson et al., 2015), and hydrothermally deposited secondary minerals are also present on the floor of the salt plain, particularly south of Dallol near Black Mountain (Figure 1). Black Mountain is a small hill composed of salt rich in hematite (e.g., Franzson & Helgadóttir, 2012) and is characterized by geothermal manifestations, extensive precipitation of bischofite minerals, and an acid pool called Black Pool (Figures 1c–1i; Figure S1 in Supporting Information S1). This area is also inferred to have been created by a phreatic eruption (Siebert et al., 2010). Dallol and the nearby surroundings are a potential geothermal resource with an estimated reservoir temperature of over

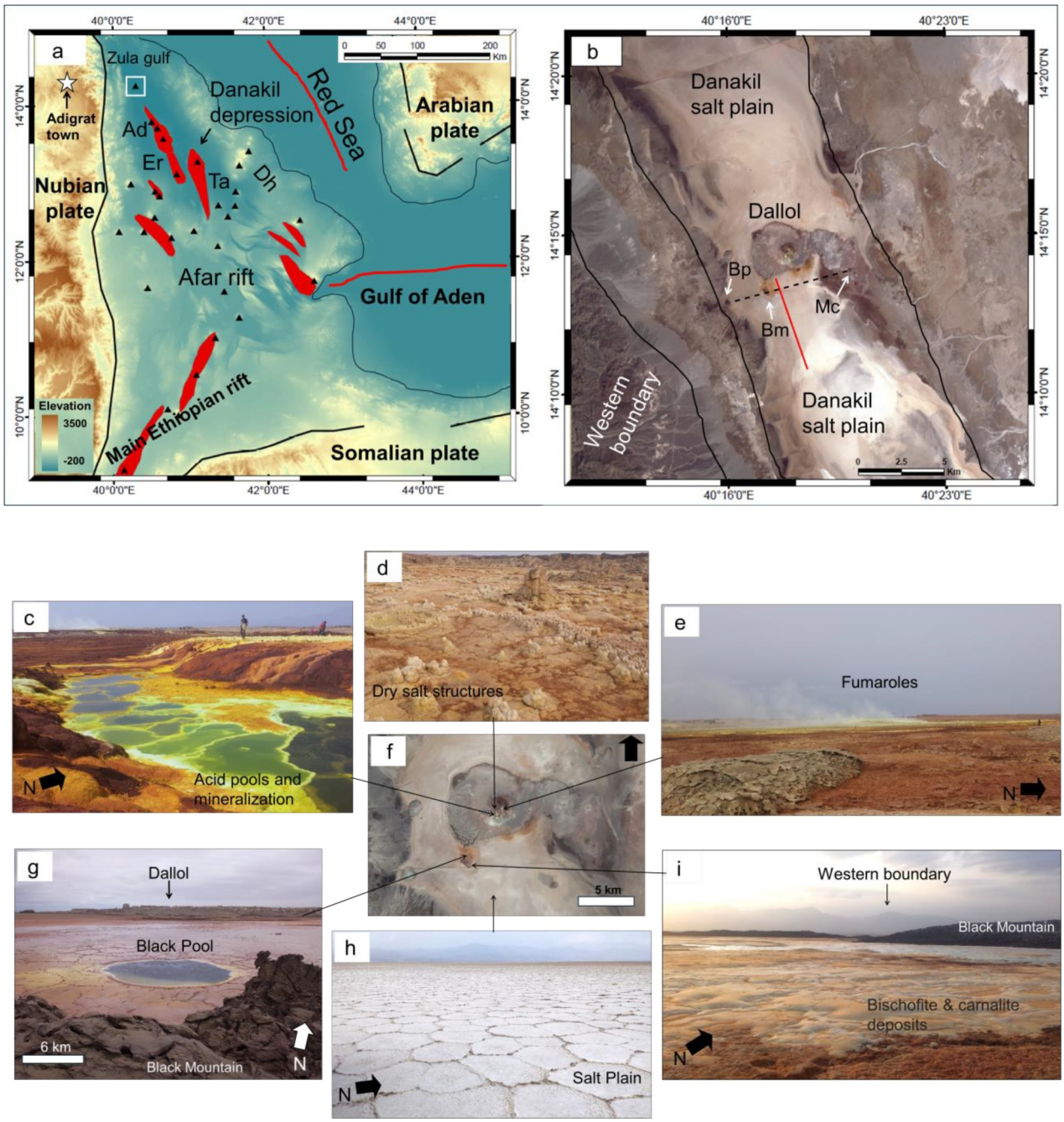

Figure 1. (a) Map of the northern East African Rift system including Afar and the northern Main Ethiopian Rift. Red oval outlines the mark the magmatic segments, and the red lines represent the offshore rifts. The black triangles represent Holocene volcanoes, and the black thick lines are the major rift boundary faults (e.g., Keir et al., 2013). Volcanic segments are Alu-Dalafilla (Ad), Erta Ale magmatic segment (Er), Tat Ale (Ta) and the Danakil Horst (Dh). The white rectangular box marks Dallol within the Danakil depression as shown in panel (b). (b) Spot-5 image of the Dallol area; Bubbling Pool (Bp); Black Mountain (Bm); and mud crater (Mc). The red line represents the 2004 dike intrusion (Nobile et al., 2012), and the black dashed line marks WEW-oriented inferred transverse fault. Pictures of: (c) Brine pools, (d) dry salt structures and hot spring vents, (e) fumarole activity inside the Dallol crater, (f) aerial map of the area displaying the locations where the pictures were taken. (g) The Black Pool near the Black Mountain, (h) salt plain and (i) secondary salt precipitation of Bischofite and Carnallite deposit. All pictures were taken in 2018.

280°C (e.g., Franzson et al., 2015; Varet et al., 2012), but there is no active geothermal energy exploitation in the area so far.

The stratigraphy of the Dallol salt plain has been constrained from boreholes that have been drilled to a maximum depth of 960 m. They show extensive evaporite sequences with tens of m thick potash rich bed (named Houston

Formation by the Potash Industry) near the base of the Dallol Formation (Foubert et al., 2024). The Dallol Formation extends from the surface to 500–900 m depth within the basin center (Bastow et al., 2018; Foubert et al., 2024). The top half comprises interbedded halite, clays, silts and fine carbonates (named Clastic Overburden by the Potash Industry), followed in the lower half by mainly halite (named Upper Rock salt and Lower Rock Salt, respectively, above and below the Houston Formation by the Potash Industry) (Foubert et al., 2024). In addition, a thin (∼20 m thick) bed of basalt fragments of uncertain origin has also been encountered in one of the boreholes at a depth of 170 m.

Ground motion and seismicity measurements show that Dallol is magmatically and tectonically active. In 2004, an InSAR and seismicity study showed that a dike intrusion occurred south of Dallol (Figure 1b), associated with 30 cm of subsidence at Dallol in relation to deflation of a 2.4 km deep magma chamber directly under the volcano (Nobile et al., 2012). This was the first time that deformation caused by magma movements was observed in the area and led to the interpretation that Dallol is a nascent volcano. Since the dike intrusion, no deformation was measured at Dallol until subsidence suddenly started in 2008, coeval with the Alu-Dalafilla eruption 50 km to the south (Battaglia et al., 2021; Pagli et al., 2012). The subsidence has been continuing to date. InSAR measurements during 2008–2010 showed subsidence at Dallol volcano at a rate of 100 mm/yr, which was attributed to a source located at a depth of 0.5–1.5 km (Battaglia et al., 2021). Since then, Albino and Biggs (2021) show that between 2015 and 2020, subsidence continued at Dallol at a rate of up to 33 mm/yr. The presence of a magmatic body below Dallol is also supported by the presence of positive gravity and magnetic anomalies in the area (UNDP, 1973).

2. InSAR Data Processing and Time Series Analysis With π-RATE

We produced interferograms from 280 acquisitions between 2014 and 2023 from the Sentinel-1A/B SAR satellites of the European Space Agency in both ascending (track 014) and descending (track 079) satellite tracks. Interferograms were created using the open-source software InSAR Computing Environment (ISCE) version 2 (e.g., Gurrola et al., 2010) (see Figure S2 in Supporting Information S1). For all the interferograms, multi-look (averaging of adjacent pixels) was applied. We used a standard multi-look of 7 by 19 pixels in the azimuth and range directions, respectively, where the azimuth direction is the flight direction of the satellite, and the range direction is perpendicular to it. The 1-arcsec SRTM-DEM (Shuttle Radar Topography Mission-Digital Elevation Model) was used to remove the topographic phase in InSAR processing and for geocoding (Farr et al., 2007).

Phase unwrapping was performed using the integrated correlation and unwrapping (ICU) branch cut method (Goldstein et al., 1988). We constructed a total of 490 interferograms from both satellite tracks with a minimum of 12 days of time gap between acquisitions (temporal baseline) and a maximum of about 238 days. We used perpendicular baselines of a maximum of 160 m (Figure S3 in Supporting Information S1).

The unwrapped geocoded interferograms from both ascending and descending tracks were multilooked to a final pixel size of 90 m-by-90 m before being analyzed with the π-RATE (poly-interferogram rate and time series estimator) software to obtain average velocity maps and time series of incremental Line-of-Sight (LOS) displacements (Wang et al., 2012). For the π-RATE analysis we selected an area centered at Dallol volcano and extending 15 km to the north and south and 9 km to the east and west. π-RATE is a software used to minimize errors in the interferograms (i.e., atmospheric and orbital errors) using a network-based approach, and to invert the interferograms using a least-squares method for the average velocity, time series of incremental and cumulative displacements and their associated uncertainties (e.g., Biggs et al., 2007; Elliott et al., 2008; La Rosa et al., 2024; Pagli et al., 2014; Wang et al., 2012). For the reference area, π-RATE automatically selects the average reference plane that represents a stable and undeformed region. π-RATE also identifies and removes residual unwrapping errors using the phase closure technique (Wang et al., 2012; Yang et al., 2024) prior to time series analysis and inversion. In π-RATE a continuous network of non-redundant interferograms, called a Minimum Spanning Tree (MST, Kruskal, 1956), can be defined by selecting interferograms that have either the smallest noise variance (less noisy interferograms) or the highest number of coherent (reliable) pixels remaining after unwrapping.

We applied orbital corrections and atmospheric noise filtering epoch by epoch. For the orbital error estimation, a planar model was applied (Biggs et al., 2007), and to remove the topographically correlated atmospheric delay error, we used the 1-arcsec SRTM DEM (Elliott et al., 2008). We applied atmospheric phase screen (APS) filtering over the temporally and spatially varying turbulent component of the atmospheric delay errors (Ferretti et al., 2001; Hanssen, 2001), which leads to reduced noise levels. This is done by using a Gaussian temporal high-

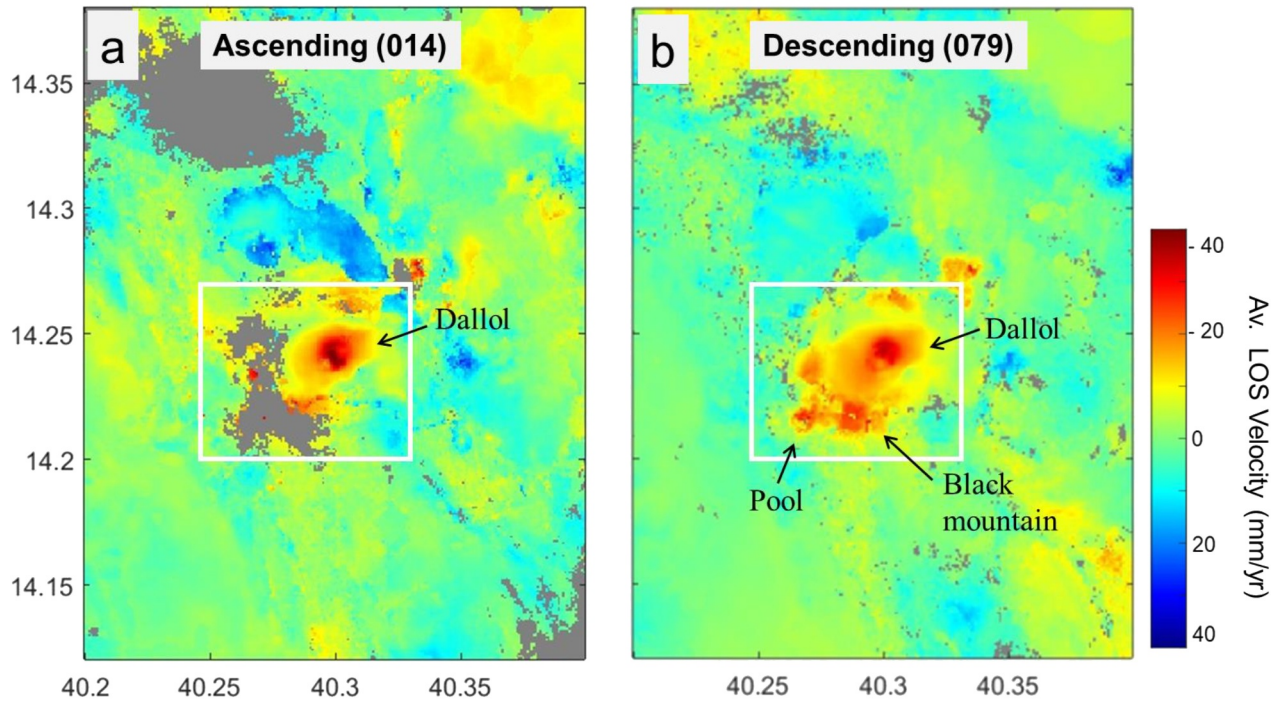

Figure 2. Average LOS velocity maps of the Dallol study area and its surroundings. In (a) is the ascending track (014) and descending track (079) in (b). The deformation region modeled in this study is indicated with a white rectangle.

pass filter with 1σ of 0.5 years, and a low pass Butterworth filtering of spatially correlated noise. The APS filtering was not applied for the velocity map inversion, but only for the time series. Tests in π-RATE including the effects of APS filtering applied on the velocity maps to reduce the noise are explained in Section 2.1 and results are compiled in Figures S4–S9 and S11–S13 in Supporting Information S1. We estimated the variance-covariance matrix using a 1-D covariance function (Hanssen, 2001; La Rosa et al., 2024; Pagli et al., 2014; Wang et al., 2012). For the time-series inversion, a Laplacian smoothing factor was used after APS filtering. We selected a smoothing factor that minimizes the trade-off between solution roughness and residual sum of squares of the displacement (L-curve in Figures S10a and S10b in Supporting Information S1). We finally estimated the general weighted least squares average velocity and its uncertainties using the variance-covariance matrix method to consider the spatial and temporal correlation between interferograms (Wang et al., 2009). For the final velocity maps, we fix thresholds of the number of coherent pixels as well as the RMS (Root Mean Square) misfits for both ascending and descending tracks.

To reduce the noise and incoherent pixels in the final average velocity maps of both tracks, particularly the ascending track, several tests were performed in π-RATE by setting different parameters with varying values as discussed in Section 2.1.

2.1. Noise Filtering With π-RATE

We perform noise filtering over the processed average Line-of-Sight (LOS) velocity maps of both tracks in order to smoothen the noise and minimize the difference in the values of the deformation velocity between the two tracks.

The average Line-of-Sight (LOS) velocity maps indicated the presence of at least three concentric deformation signals at Dallol volcano, Black Mountain, and Bubbling Pool, consistent with subsidence, with the main subsidence signal situated on the crater of Dallol volcano (Figure 2). The deformation signals at Dallol show different maximum LOS rates (consistent with subsidence) in the two tracks: 35 mm/yr in the descending track and 43 mm/yr in the ascending track. We attribute the difference to the fact that the ascending track is noisier than the descending track, as also shown by the generally less smooth average velocity map and relatively higher RMS misfit values (Figure 2, Figures S4–S13 in Supporting Information S1).

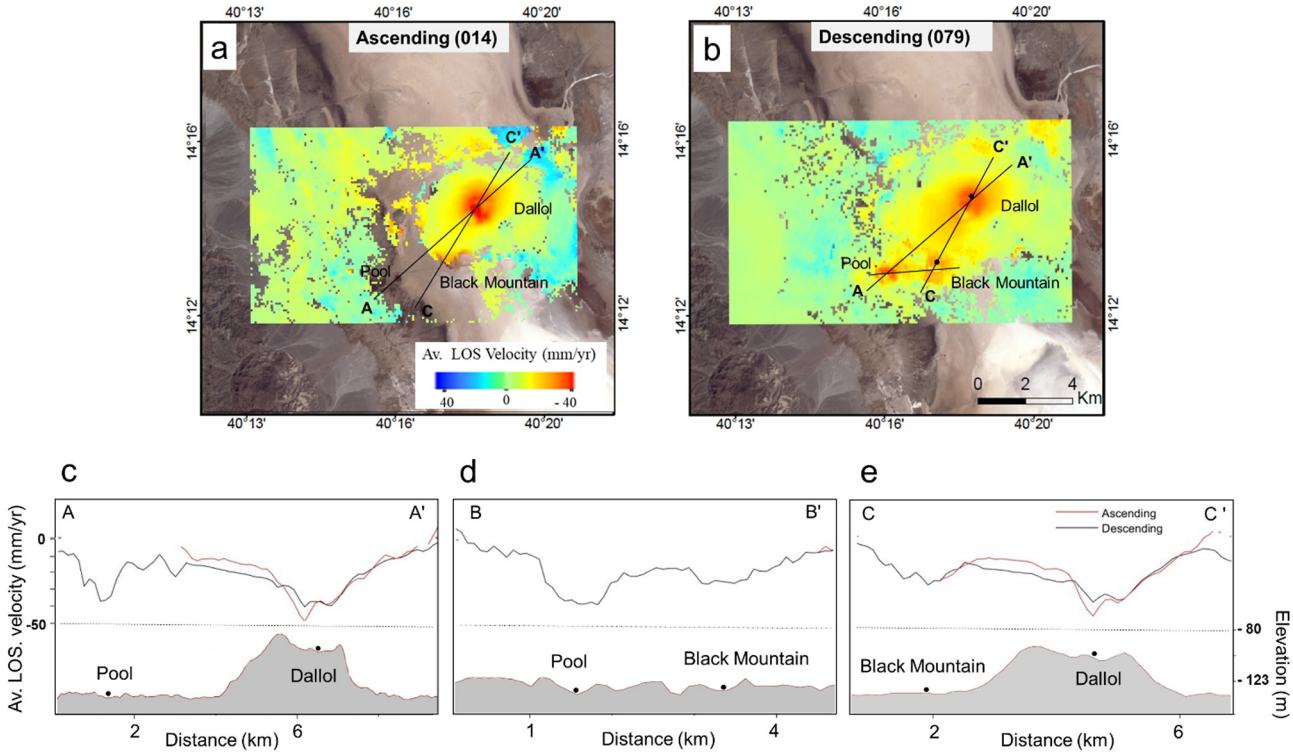

Figure 3. Observed average LOS velocity maps of Dallol and its surroundings from ascending (014) (a) and descending (079) (b) tracks. The black lines in (a and b) represent cross-sections shown in (c–e), and black dots mark the locations of pixels whose time-series is shown in Figure 4. (c–e) Show LOS velocity cross-sections across the ascending and descending velocity maps. The black dots on the elevation profile in panel (c–e) indicate the locations of the deformation signals.

To best filter the noise, several tests were conducted in π-RATE. The results showed that velocity maps are smoother and more consistent in both tracks without the application of the APS filtering. We also tested the effect of applying different methods of interferogram selection for the construction of the MST. We tested both the minimum noise variance and the highest number of coherent pixel methods, and the results are comparable for the descending velocity map. For the ascending track, there is an increase of 2 mm/yr velocity at the center of Dallol when using the highest number of coherent pixels method (Figures S4–S7 in Supporting Information S1).

We also tested the effect of using different thresholds of the RMS misfit and minimum number of coherence pixels on the average velocity maps. For the RMS misfit threshold, we tested values between 2 and 1 mm/yr for both tracks. An RMS misfit of 2 mm/yr maintains good coverage on Dallol for the descending track, but for the ascending track, such a threshold does not fully remove noisy patches on top of Dallol, likely due to residual unwrapping errors. Lowering the RMS threshold to 1 mm/yr results in removing most of the deformation signals (Figures S11–S14 in Supporting Information S1). We tested different values for the threshold of minimum number of coherent epochs in the velocity maps ranging from 10 to 90 and found that only a few pixels are removed using 90 epochs (see Figures S6–S9 in Supporting Information S1). Finally, we manually identified and removed interferograms that have unwrapping residual errors from the ascending track once again and then performed the above tests to find the most robust velocity map to model.

For the modeling we chose a solution obtained by setting relatively conservative thresholds (Figure 3). The RMS misfit threshold was set to 2 mm/yr, the coherence thresholds were set to 50 epochs, and the APS filter was not applied. Using these parameters meant that Bubbling Pool and Black Mountain are not coherent in the ascending track, and only coherent in the descending track. However, we believe that all three subsidence signals are real as they are present in most of the tests. The same conservative thresholds were set for the time series calculation, and we obtained continuous cumulative time series for selected sites on Dallol and Black Mountain for the descending track only, while coherence was lost at Bubbling Pool.

3. InSAR Results and Modeling

3.1. InSAR Results

Average LOS velocity maps and time series of displacements with their uncertainties have been obtained for both ascending and descending Sentinel tracks (track 014 and track 079). The main subsidence signal at Dallol volcano is slightly elongated north-east with a radius of ~0.8 km (Figures 3a and 3b). Two other local maxima south and south-west of Dallol volcano correspond to the Bubbling Pool and Black Mountain areas with a radius of ~0.5 and 0.6 km, respectively (Figures 3a and 3b).

Cross-sections across the average LOS velocity maps of both tracks confirmed that the deformation signals at the three sites have similar deformation patterns, but the maximum LOS velocity in the ascending track is higher than that in the descending track (Figure 3). At Dallol volcano, the maximum subsidence at its center is 35 mm/yr in the descending track and is up to 43 mm/yr in the ascending track (Figures 3c and 3d). The maximum subsidence at Bubbling Pool is 34 mm/yr, and at Black Mountain is 23 mm/yr in the descending track (Figures 3c–3e).

Overall, the velocity maps show that the highest RMS misfit (the misfit between the observed and predicted) is along the rift zone, including the area about 13 km north of Dallol along the axis of the rift, where the lowest coherence is also recorded (Figures S4–S13 in Supporting Information S1). The salt plain north and south of Dallol always shows a signal of range decrease, likely due to propagation effects of the SAR signal in the salt deposits.

Near the deforming centers, the higher RMS values are mainly focused near the Bubbling pool. The maps of the RMS misfit for both tracks show relatively higher misfits on the rift axis and lower values on the rift flanks. This is likely caused by the rift flanks being more coherent surface compared to the rift axis where rapid changes in the surface characteristics occur due to salt evaporation and precipitation, leading to loss of coherence.

In order to assess the time-evolving style of the deformation, we examined the time series of cumulative displacements from the descending track as this offers less noise than the ascending track and has the highest number of coherent pixels in the center of the two subsidence signals at Dallol (Figure 4a) and at Black Mountain (Figure 4c).

Both the input data (red plus signs in Figure 4) and the final smoothed time series (black dots in Figure 4) show good agreement, and all the time series show a continuous LOS range increase throughout the entire observation period (Figure 4). We also calculated the detrended time series (Figure 4) to better highlight any possible fluctuation or deviation from a linear trend. From this we find that at Dallol volcano the subsidence velocity was faster than a linear trend at the beginning of the observation period to mid-2019, suggesting the rate of subsidence is decaying through time (Figure 4a), while at Black Mountain no long-term variation with respect to a linear trend is observed. Both detrended plots also show annual fluctuations of a few mm/yr, with the peaks and troughs occurring at the same time in both locations. In order to understand whether these fluctuations are related to seasonal processes rather than residual atmospheric artifacts, we also show in Figures 4a and 4b the annual precipitation data between 2015 and 2022, but no clear correlation is found. The data are for the station on the plateau margin near Adigrat town (https://power.larc.nasa.gov/data-access-viewer/) as the ground water in Dallol comes from the nearby highland to the west (UNDP, 1973). The Dallol region has a desert climate with only limited annual rainfall, but the area is seasonally flooded by meteoric water that originates from the western escarpment and marginal grabens (UNDP, 1973), where the rainy season is between June and September (e.g., Demissie et al., 2015; Meaza et al., 2017). This leads to annual flooding (generally June–September) of the rift valley floor around Dallol by several cm of water.

3.2. InSAR Velocity Modeling

To model the deformation at Dallol, we applied a joint inverse modeling of the average velocity maps from both ascending and descending satellite tracks, assuming three Okada rectangular dislocations (Okada, 1985) in a homogeneous isotropic and elastic half space with a Poisson's ratio of 0.25. Since the deformation source in Dallol is shallow (0.5–1.5 km) depth, we prefer to use a finite source such as an Okada source rather than a point source such as a Mogi source. Also, the Okada sources were assumed to be horizontal (a sill). The Okada rectangular dislocation sill model is used to study the ground deformation caused by the closing and opening of the sources that are represented in a rectangular shape. The opening of the Okada source corresponds to inflation, such as an

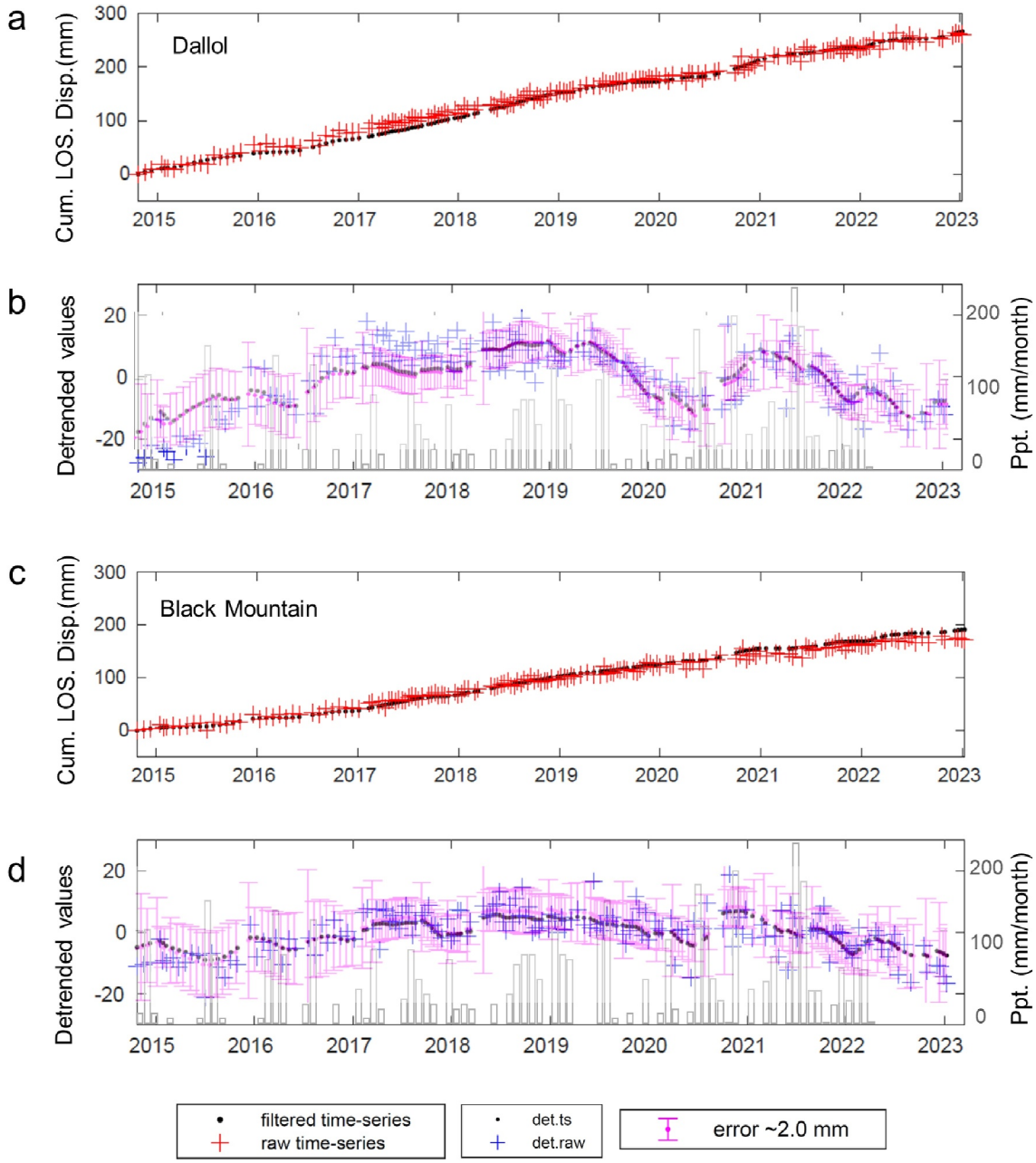

Figure 4. Time series of cumulative LOS displacement for the descending track at Dallol (a), at the Black Mountain (c), with the corresponding detrended plot in (b) and (d), respectively. See Figure 3 for the locations of the pixels. The year labels are ticked for the start of each year. The red plus signs are the input data and blue plus signs are detrended data. The black dots are the final smoothed time series, and the pink lines represent the error bars. The histograms in the detrended plots are the annual precipitation (mm/month).

increase in fluid pressure, magma inflow, or thermal expansion. In contrast, closing of the source corresponds to subsidence from processes such as pressure decrease, degassing, or magma solidification.

The modeling was conducted using an optimization approach based on Monte Carlo Simulated annealing followed by a derivative-based algorithm (e.g., Cervelli et al., 2001; Wang et al., 2014). To conduct the inversion efficiently, we subsampled data by applying a quadtree algorithm (Jonsson et al., 2002; Wang et al., 2014) to the velocity maps (Figure S14 in Supporting Information S1).

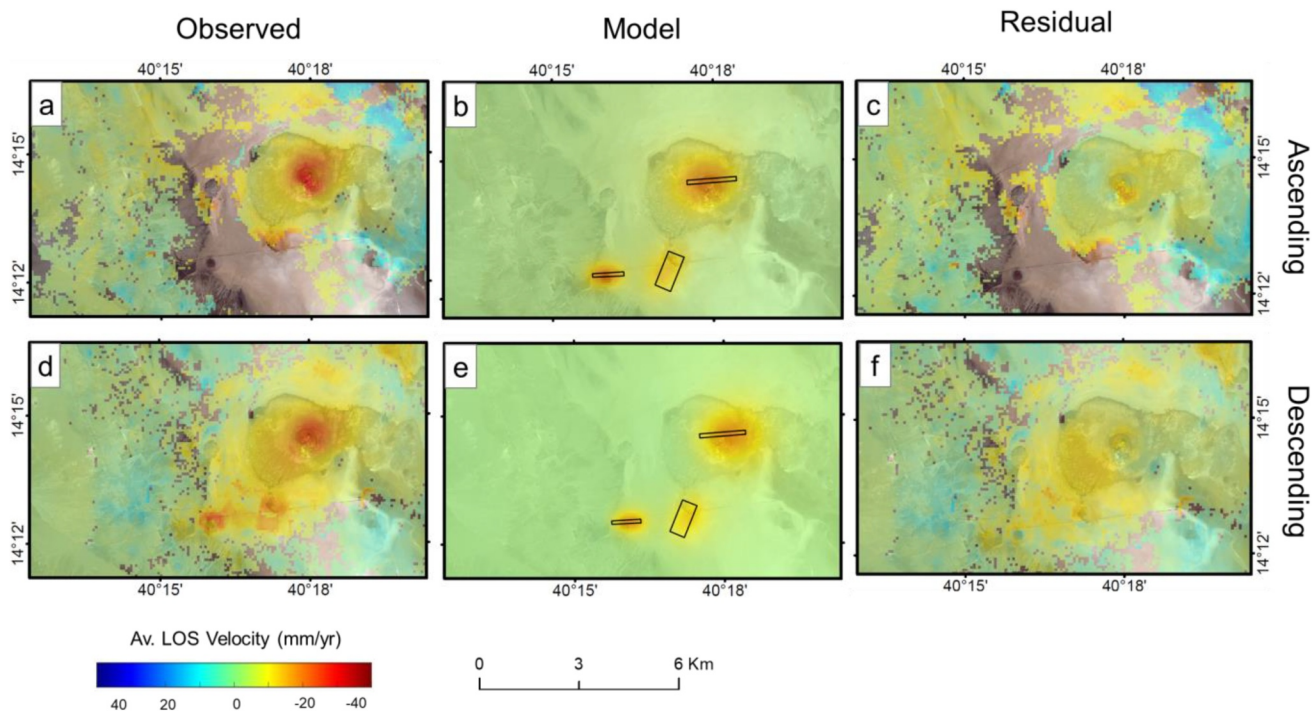

Figure 5. Observed LOS velocity maps for ascending (a) and descending (d) tracks, model LOS velocity maps for ascending (b) and descending (e) tracks and residual LOS velocity maps for ascending (c) and descending (f) tracks draped over the Spot-5 image. Surface projections of the inferred best-fitting rectangular Okada source models are shown in black rectangles in (b) and (e).

The modeling results (Figure 5 and Table 1) reveal that the best-fit source at Dallol is at a depth of 1.5 km below the center of the volcano. It has horizontal dimensions of 1.7 km by 0.16 km, with a contracting rate (thickness) of 0.7 m/yr. In contrast, sources at the Bubbling Pool and at Black Mountain are smaller in size, and at shallower depths, 0.6 and 1 km depth, respectively (Figure 5 and Table 1). Models are assumed to be horizontal without dip, and their orientation is given in Table 1.

To estimate the uncertainties on the best-fitting source parameters, we used a Monte Carlo simulation of correlated random noise (Wang et al., 2014). For each ascending and descending velocity map, we generate 100 simulations of spatially correlated random noise based on its variance-covariance matrix, then each of these simulations is added to the respective velocity map and the maps are inverted individually. Hence, we obtain 100 different model solutions, and the uncertainties are then obtained by calculating the 90% confidence interval of the solutions. The distribution of parameters of the three sources and their 90% confidence interval are shown in Figure S15 in Supporting Information S1.

Table 1
Best-Fit Parameters of Okada Sources With Their 90% Confidence Interval (CI) at Bubbling Pool, Dallol Volcano, and Black Mountain

	Source parameters							
Deformation signal	Longitude (°)	Latitude (°)	Depth (km)	Length (km)	Width (km)	Opening (m/yr)	Strike (°)	Volume change (m^3/yr)
Dallol	40. 2993	14.2439	1.5	1.67	0.16	0.7	84	-1.8×10^5
90% CI	40.2983–40.30	14.2434–14.2441	1.3–1.6	1.28–2.3	0.1–0.2	0.63–0.78	73–90	
Bubbling pool	40.2672	14.2155	0.63	1.04	0.13	0.3	87	-4×10^4
90% CI	40.267–40.2674	14.2153–14.2156	0.56–0.63	1–1.13	0.1–0.3	0.1–0.4	81–91	
Black Mountain	40.2862	14.2164	1	1.2	0.57	0.08	22	-5.5×10^3
90% CI	40.2858–40.2866	14.216–14.2167	1	1.1–1.3	0.26–0.75	0.07–0.18	15–33	

Note. The volume change values are calculated results of the model parameters. The locations (Longitude & Latitude) represent the center of each Okada source models.

Overall, the source parameters are relatively well constrained within narrow intervals. The depth of the Dallol source falls within the interval of 1.3–1.6 km, the length 1.1–2.4 km, and the width 0.1–0.2 km. For the source at the Bubbling Pool, the parameters again show a narrow range of confidence intervals. The source depth ranges between 0.5 and 0.7 km, the length is 0.9–1.1 km, and the width is 0.1–0.3 km. Intervals of uncertainty at the Black Mountain source have an intermediate range between the other two sources. It has a depth of 1 km, length and width of 0.9–1.4 km and 0.1–0.2 km, respectively (Figure S15 in Supporting Information S1).

In addition, the marginal posterior probability distributions of the model parameters show that some parameters show clear trade-offs between each other, such as depth with length and orientation, and length with orientation in Bubbling Pool and Dallol sources. Trade-offs of depth with opening and width are also observed in the Bubbling Pool. Trade-offs are also seen in the Dallol source of location with depth, length, and orientation. At Black Mountain, the trade-off is between the depth and opening of the source.

4. Discussion

The use of numerous and coherent interferograms spanning a period of 9.5 years allowed the identification of deformation due to three sources: Dallol volcano, Black Mountain and the Bubbling Pool, with the sources modeled as contracting Okada dislocations at shallow depths of 0.6–1.5 km. Previous studies, such as the InSAR modeling of the 2004 intrusion event and coeval subsidence at Dallol volcano (Nobile et al., 2012) coupled with magnetotelluric (MT) magnetic and gravity surveys, indicate the existence of a shallow heat source (magma intrusion) at Dallol (UNDP, 1973; Vilhjalmsson et al., 2012).

4.1. Subsidence at Dallol Volcano

The center of the Dallol volcano is known for its various salt formations and the intense hydrothermal activity in the evaporites. Additionally, hot springs and fumaroles also characterize the surface. We measure a subsidence rate of up to 35 mm/yr in descending LOS during the 2014–2023 period in the center of Dallol. A previous Sentinel study found a similar rate in descending LOS of up to 33 ± 1 mm/yr, albeit near the center of Dallol, between 2015 and 2020 (Albino & Biggs, 2021). The LOS velocity in the ascending track cannot be compared to past results as it has not been reported in the literature.

The best-fitting parameters from the joint inversion of ascending and descending tracks showed that ground subsidence at Dallol volcano can be explained by a sill shaped contraction volume at a depth of 1.5 km and a volume decrease of 1.8×10^5 m^3/yr (Table 1). Our modeled source is shallower than the magma reservoir at 2.4 km depth modeled to have fed the 2004 dike (Nobile et al., 2012) but comparable to the models (0.5–1.5 km depth) suggested by Battaglia et al. (2021) for the 2008–2010 subsidence period. We compared our modeled source to the MT derived image in the area and found that it falls below the shallow highly resistive zone and is instead within the low resistivity (conductive) region (Figure 6). The low resistivity anomaly is consistent with the presence of connected partial melt in the magmatic heat source, and we therefore interpret the deformation source to be a magmatic sill. In contrast, the shallower highly resistive anomaly that is above the modeled sill is consistent with the shallowest few hundred meters being the zone of hydrothermal activity (steam or anhydrite deposits) above the magmatic heat source (Vilhjalmsson et al., 2012).

The LOS time series plots at Dallol showed a linear range increment with small wavelength (annual) and amplitude variations (Figure 4) but superimposed on a longer wavelength variation, suggesting that the rate of subsidence is decreasing. This temporal pattern is also consistent with the previous Envisat study showing higher subsidence rates up to 100 mm/yr in the earlier 2008–2010 period (Battaglia et al., 2021). Given that the magma reservoir below Dallol volcano that fed the 2004 dike was at 2.4 km depth and also within the low resistivity zone, we interpret the ∼1.5 km deep sill the 2014–2023 subsidence as being near the top of the same reservoir network. In our deformation maps, we see no evidence of magma outflow from the sill, such as the emplacement of a nearby dike or corresponding nearby uplift. Therefore, we interpret the decaying subsidence at the Dallol volcano to be possibly related to cooling and contraction of the top of a magma body/lens.

4.2. Subsidence at Bubbling Pool and Black Mountain Areas

The subsiding Black Mountain and Bubbling Pool areas are closely spaced, less than 2 km apart, and their modeled deformation sources are located at 1 and 0.6 km depth, respectively. To interpret the origin of the

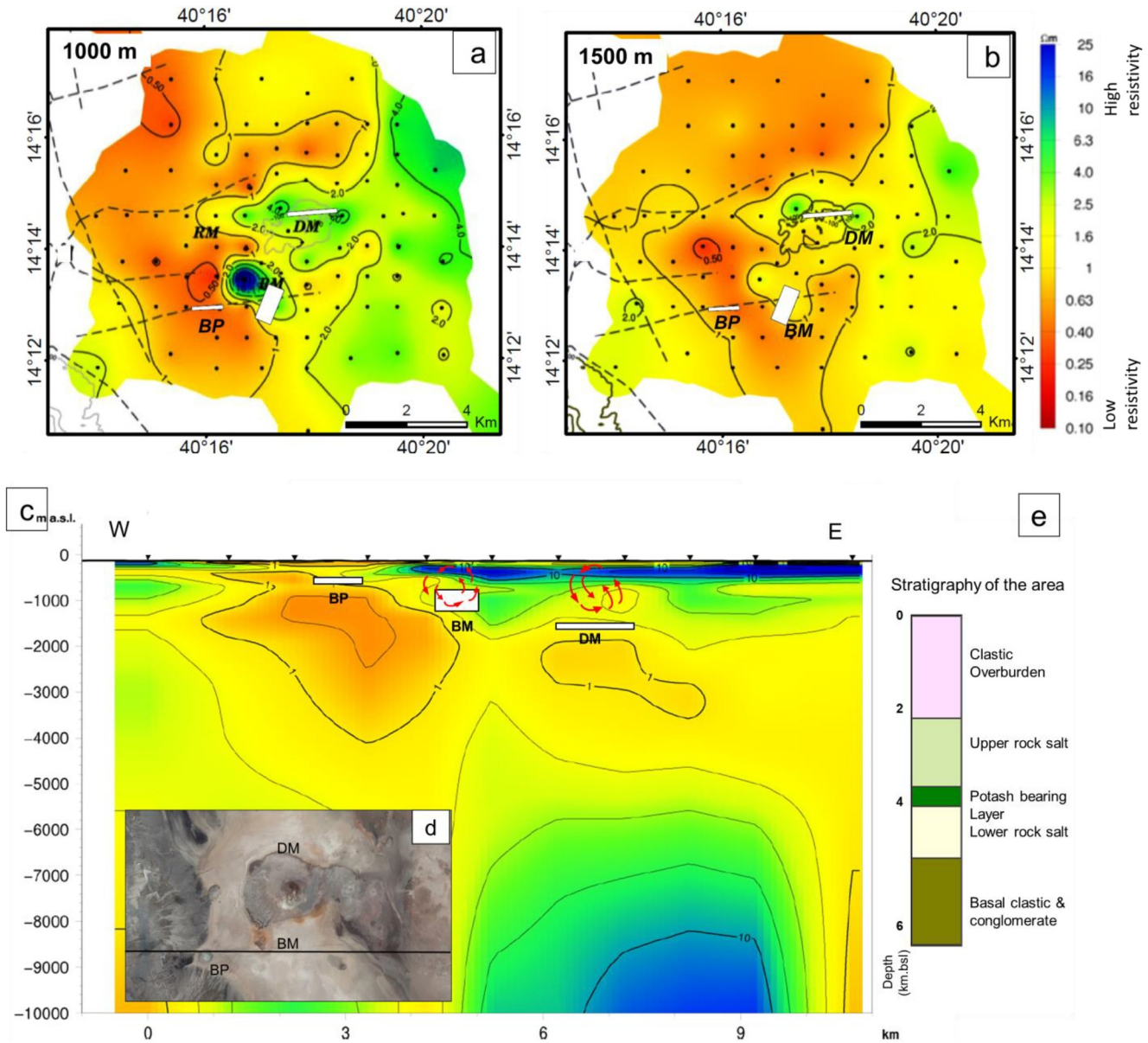

Figure 6. Inferred resistivity map of the Dallol volcano and its surroundings at 1,000 m (a) and at 1,500 m (b) below sea level, and the E-W profile section (c). The profile line (black line) in the image (d) represents the profile section reproduced from Vilhjalmsson et al. (2012). The black dots in A and B are the MT-stations. (e) Stratigraphic section of the Dallol area, adapted from Foubert et al. (2024). The rectangles with white fillings represent the Okada sources. The symbols are DM- Dallol Mountain; BM- Black Mountain; BP- Bubbling Pool; and RM- Round Mountain. The color scale displays resistivity values from higher (25 Ωm) to lower (0.1 Ωm), which also corresponds to lower to higher conductivity, respectively.

subsidence, we compare our models to the MT derived resistivity images. These show a shallow concentric highly resistive area at the northeastern corner of the subsiding Bubbling Pool and beneath the Black Mountain area (Figure 6a). The high resistivity continues to ∼1,100 m bsl depth below Black Mountain (Figure 6), coinciding with our InSAR derived source model situated at ∼1 km depth. The resistivity structure here is most consistent with high temperature hydrothermal activity/presence of a steam column, and we therefore interpret the subsidence at Black Mountain as potentially being caused by pressure changes within the shallow hydrothermal system.

Since ground water at Dallol is mostly meteoric in origin (UNDP, 1973), one might expect the highly seasonal rainfall to be expressed in hydrothermal related ground motions. Our observations of the subsidence at Black Mountain show short wavelength temporal variability superimposed on a long-term linear subsidence. However,

the changes seen on the time series plot do not clearly follow the seasonal variations of the rainfall (Figure 4). This indicates that the surface water from the annual flooding (generally June–September) of the rift valley floor does not rapidly migrate subsurface, an interpretation consistent with the low permeability of the evaporite rock type, which dominates the hydrothermal zone (Warren, 2015).

At the Bubbling pool, the MT image shows layers of low resistivity that extend from the surface down to deeper levels (~6 km; Vilhjalmsson et al., 2012). This can possibly indicate the presence of hydrothermal activity that is not boiling below the pool, unlike Dallol and Black Mountain, as boiling systems show high resistivity. This possibly agrees with the location of the pool at the periphery of the geothermal outflow region. In addition, field measurements show that the pool is at a low (ambient) temperature (Lopez-García et al., 2020). Another explanation could be the presence of low resistivity and a secondary low temperature clay mineral assemblage as it is located at the boundary between the salt plain and the sedimentary bed.

The spatial arrangement and orientation of the Black Mountain and Bubbling Pool deformation sources potentially point toward a strong structural control on subsurface fluid flow. A noticeable observation is that these 2 deformation sources align along a strike of ~75°E, which also aligns with the Mud Crater positioned ~3 km to the east (Figure 1). The ~75°E strike is parallel to the strike of elongation of the Bubbling Pool source, and parallel to the transverse rift faults commonly inferred in structural mapping, and potential field geophysical surveys of the Dallol area (UNDP, 1973; Vilhjalmsson et al., 2012) and directly observed in seismic reflection images (e.g., Bastow et al., 2018). The observations support an interpretation that these manifestations of subsurface fluid flow have developed along a single transverse fault, along which there is the flow of hydrothermal fluid. The interpretation has the implication that rift transverse faults are important in contributing to fracture permeability in the hydrothermal system.

In addition to the a cross-rift faults, the along rift faults outlined from the seismic reflection study (e.g., Bastow et al., 2018) showed that Dallol volcano and Black Mountain are within the innermost set of basin faults, while the Bubbling Pool is toward the edge of the basin and on the footwall side of a major (several hundred m displacement) east dipping normal fault that strikes parallel to the rift. This implies that the subsidence took place in the same hydrothermal aquifer at the Bubbling Pool and Black Mountain that has been faulted at different depths eastward. This phenomenon illustrates the appearance of two distinct narrow zones of depressurizing hydrothermal/steam columns above the contracting heat source, where the fracture interconnection allows them to share a heat source.

4.3. Interactions Between Evaporites and Magma

Ground motion related to hydrothermal processes is mostly interpreted as caused by subsurface pressure changes. However, the presence of the evaporite dominated stratigraphy within the depth range of Black Mountain and Bubbling Pool deformation sources raises the possibility that subsidence is caused by the dissolution of the hydrated evaporite layer where localized hot fluid flow occurs. The surface mineralization suggests this is a feasible process. Secondary salts such as bischofite are observed around the surface of Black Mountain (Figures 1f and 1h), which can be only reasonably explained as being sourced from dissolution of the subsurface hydrous salt horizon/s within the evaporite sequence. In the Danakil depression, the hydrated salt layers within the Potash rich layer (e.g., carnallite, kainite) are susceptible to dissolution (Warren, 2015) and therefore are likely candidate member beds for localized horizontal fluid migration and accompanied volume loss by being dissolved. This interpretation is consistent with the depth estimates of the Potash rich formation from the boreholes and visual inspection of seismic reflection data. The seismic images show that the Potash rich layer is in the depth range ~400–800 m near the western boundary of the rift corresponding to the Bubbling pool, and then down-faulted by the dominant NNW striking basin bounding faults and therefore deepens eastward toward Black Mountain to a range of ~800–1,000 m depth (Bastow et al., 2018).

In contrast, at Dallol volcano, our modeled sill is deeper than the estimated depth of the Potash rich layer. The depth of our sill model therefore makes it unlikely that salt dissolution is a viable explanation.

5. Conceptual Model

Our simple schematic conceptual model illustrates the positions of the three horizontal Okada sources. The two smaller sources (located at Bubbling Pool and Black Mountain) are positioned near the shallower potash rich bed,

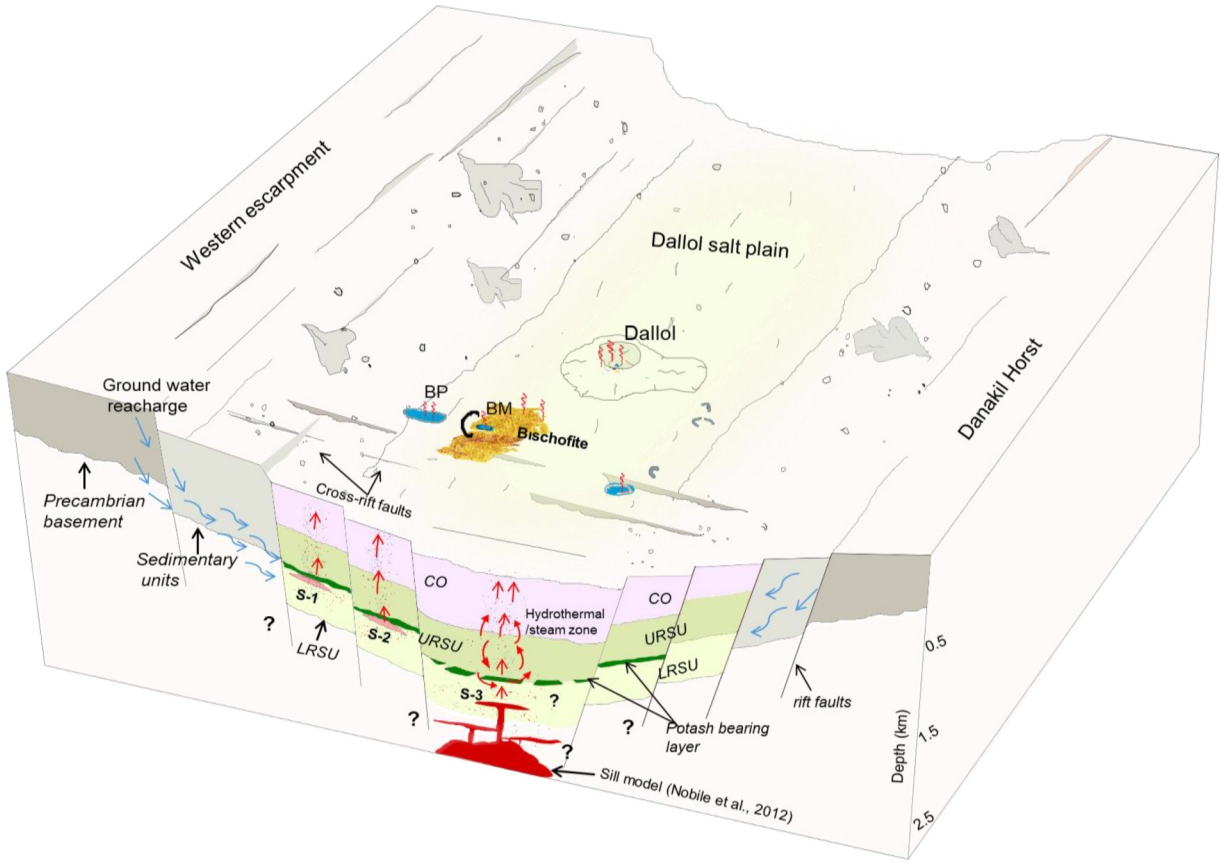

Figure 7. Conceptual model of the Dallol area showing the position of the modeled sources, along with the magmatic and hydrothermal systems. Our InSAR models are represented as S-1 (Bubbling Pool), S-2 (Black Mountain), and S-3 (Dallol). The green layer near the source models represents the potash rich layers. LRSU: lower rock salt unit; URSU: upper rock salt unit; CO: clastic overburden. Geological units are modified from Foubert et al. (2024).

while the magmatic sill at Dallol is at 1.5 km depth and connected to the 2004 magma source at 2.4 km depth and related partial melt zone. The hydrothermal zone at Dallol lies above the depth of the magmatic sill (S-3) (Figure 7). The hydrothermal system is directly recharged by meteoric water from the highlands to the west, which percolates into the rift through boundary faults and the marginal graben. The infiltrated cold water is then heated up by the sill at Dallol, located beneath the hydrothermal zone. Fluid flow and heat transfer to the Bubbling Pool and Black Mountain systems is facilitated by the ~EW striking cross-rift faults as well as the rift parallel faults. Intersection of the rift parallel and the cross-rift faults, where permeability is highest, plays an important role in facilitating the ascent of the hot geothermal fluids to the surface.

6. Conclusions

An InSAR survey from Sentinel-1A/B at the Dallol area during 2014–2023 has identified the presence of three concentric subsidence signals that are ~2 km apart and coincide with the Dallol volcano, Black Mountain, and Bubbling Pool. The signals are continuous and linearly subsiding at varying rates, with a maximum subsidence rate of 35–43 mm/yr at Dallol volcano. Horizontal Okada dislocation models revealed the location, depth, and geometries of the three subsiding signals. The shallowest deformation source is below the Bubbling Pool between 0.5 and 0.7 km depth, while the deepest source is below Dallol volcano at a range of 1.3–1.6 km. We interpret the subsidence at Dallol volcano as caused by magmatic cooling and contraction near the top of the previously identified magma reservoir from both the MT and InSAR models of prior magma activity. On the other hand, our modeled Okada sources at the Black Mountain and Bubbling Pool are in the hydrothermal zone interpreted from MT data and can be better explained by either a progressive pressure decrease in the hydrothermal circulation/steam zone and/or by dissolution of potash rich salt by the hydrothermal fluids. Salt dissolution is potentially particularly relevant at Black Mountain, where potash rich salt mineralization is observed at the surface.

Inclusion in Global Research Statement

The study is conducted in the Dallol area in the Afar regional state, Ethiopia. We have collaborated with a local researcher, EL from Addis Ababa University in the manuscript review and validation as well as the corresponding author, BK. We believe that our research has made an immense contribution to the region and our collaboration benefits the global research community.

Data Availability Statement

The European Space Agency's Sentinel-1 SLC's radar images are available from the open access Alaska Satellite Facility (ASF) Data Search Vertex (https://search.asf.alaska.edu/#/) and Copernicus Open Access Hub (https://scihub.copernicus.eu/). The InSAR Scientific Computing Environment (ISCE) software package-2 is open source and it is available from https://github.com/isce-framework/isce2. The π-RATE (Poly-Interferogram Rate and Time-series Estimator) open source software is available at http://www.phimaging.com/software/pirate/. The SRTM-DEM file used for interferograms and time series processing can be accessed from https://earthexplorer.usgs.gov/. The Spot-5 image used in this paper is available at https://earth.esa.int/eogateway/missions/spot. The InSAR model output, their error bars and the cumulative time series used in this study are archived in the OSF repository and available through (https://osf.io/hpzt3/?view_only=073be98bba7b4769945a03b8fcde25bf). Precipitation data used in this paper is accessed from https://power.larc.nasa.gov/data-access-viewer/. Time series analysis and modeling were performed using Matlab 2022.

Acknowledgments
This work is part of a PhD project under the XXXVII cycle of the Dottorato Regionale Pegaso in Earth Sciences; and supported by the Ministero Universit'a e Ricerca (MiUR) with the National Operational Program (PON)-2014-2020 Action IV.5 "PhDs on green issues." CP and ALR aknowledge the SpaceItUp project funded by Italian Space Agency (ASI) and Ministry of University and Research, MUR under contract n. 2024-5-E.0—CUP n. I53D24000060005. H.W. is supported by the National Natural Science Foundation of China (42274001) and the Associates Program by ICTP and the Simons Foundation (284558FY19). DK was supported by NERC Grant NE/L013509/1.

References

Albino, F., & Biggs, J. (2021). Magmatic processes in the East African Rift System: Insights from a 2015–2020 Sentinel-1 InSAR survey. *Geochemistry, Geophysics, Geosystems*, *22*(3), e2020GC009488. https://doi.org/10.1029/2020GC009488

ArRajehi, A., McClusky, S., Reilinger, R., Daoud, M., Alchalbi, A., Ergintav, S., et al. (2010). Geodetic constraints on present-day motion of the Arabian Plate: Implications for Red Sea and Gulf of Aden rifting. *Tectonics*, *29*(3). https://doi.org/10.1029/2009TC002482

Barberi, F., & Varet, J. (1970). The Erta-Ale volcanic range (Danakil Depression, northern Afar, Ethiopia). *Bulletin Volcanologique*, *34*(4), 848–917. https://doi.org/10.1007/BF02596805

Bastow, I. D., Booth, A. D., Corti, G., Keir, D., Magee, C., Jackson, C. A.-L., et al. (2018). The development of late-stage continental breakup: Seismic reflection and borehole evidence from the Danakil Depression, Ethiopia. *Tectonics*, *37*(9), 2848–2862. https://doi.org/10.1029/2017TC004798

Battaglia, M., Pagli, C., & Meuti, S. (2021). The 2008–2010 subsidence of Dallol volcano on the spreading Erta Ale Ridge: InSAR observations and source models. *Remote Sensing*, *13*(10), 1991. https://doi.org/10.3390/rs13101991

Belilla, J., Moreira, D., Jardillier, L., Reboul, G., Benzerara, K., López-García, J. M., et al. (2019). Hyperdiverse archaea near life limits at the polyextreme geothermal Dallol area. *Nature Ecology & Evolution*, *3*(11), 1552–1561. https://doi.org/10.1038/s41559-019-10050

Biggs, J., Wright, T., Lu, Z., & Parsons, B. (2007). Multi-interferogram method for measuring interseismic deformation: Denali Fault, Alaska. *Geophysical Journal International*, *170*(3), 1165–1179. https://doi.org/10.1111/j.1365-246X.2007.03415.x

Birhanu, Y., Bendick, R., Fisseha, S., Lewi, E., Floyd, M., King, R., & Reilinger, R. (2016). GPS constraints on broad scale extension in the Ethiopian Highlands and Main Ethiopian Rift. *Geophysical Research Letters*, *43*(13), 6844–6851. https://doi.org/10.1002/2016GL069890

Cavalazzi, B., Barbieri, R., Gómez, F., Capaccioni, B., Olsson-Francis, K., Pondrelli, M., et al. (2019). The Dallol geothermal area, northern Afar (Ethiopia)—An exceptional silltary field analog on earth. *Astrobiology*, *19*(4), 553–578. https://doi.org/10.1089/ast.2018.1926

Cervelli, P., Murray, M. H., Segall, P., Aoki, Y., & Kato, T. (2001). Estimating source parameters from deformation data, with an application to the March 1997 earthquake swarm off the Izu Peninsula, Japan. *Journal of Geophysical Research*, *106*(B6), 11217–11237. https://doi.org/10.1029/2000JB900399

Demissie, B., Frankl, A., Haile, M., & Nyssen, J. (2015). Biophysical controlling factors in upper catchments and braided rivers in drylands: The case of a marginal graben of the Ethiopian Rift valley. *Land Degradation & Development*, *26*(7), 748–758. https://doi.org/10.1002/ldr.2357

Doubre, C., Deprez, A., Masson, F., Socquet, A., Lewi, E., Grandin, R., et al. (2017). Current deformation in Central Afar and triple junction kinematics deduced from GPS and InSAR measurements. *Geophysical Journal International*, *208*(2), 936–953. https://doi.org/10.1093/gji/ggw434

Drouin, V., Sigmundsson, F., Verhagen, S., Ófeigsson, B. G., Spaans, K., & Hreinsdóttir, S. (2017). Deformation at Krafla and Bjarnarflag geothermal areas, northern volcanic zone of Iceland, 1993–2015. *Journal of Volcanology and Geothermal Research*, *344*, 92–105. https://doi.org/10.1016/j.jvolgeores.2017.06.013

Elliott, J. R., Biggs, J., Parsons, B., & Wright, T. J. (2008). InSAR slip rate determination on the Altyn Tagh Fault, northern Tibet, in the presence of topographically correlated atmospheric delays. *Geophysical Research Letters*, *35*(12), L12309. https://doi.org/10.1029/2008GL033659

Farr, T. G., Rosen, P., Caro, E., Crippen, R., Duren, R., Hensley, S., et al. (2007). The Shuttle Radar Topography Mission. *Reviews of Geophysics*, *45*(2), RG2004. https://doi.org/10.1029/2005RG000183

Ferretti, A., Prati, C., & Rocca, F. (2001). Permanent scatterers in SAR interferometry. *IEEE Transactions on Geoscience and Remote Sensing*, *39*(1), 8–20. https://doi.org/10.1109/36.898661

Foubert, A., Keir, D., Atnafu, B., & Kidane, T., & ADD-ON Workshop Consortium. (2024). Workshop report: Afar Dallol Drilling–ONset of sedimentary processes in an active rift basin (ADD-ON). *Scientific Drilling*, *33*(2), 207–218. https://doi.org/10.5194/sd-33-207-2024

Franzson, H., & Helgadóttir, H. (2012). *Geological and geothermal features of Dallol and surroundings. Afar region, northern Ethiopia* Iceland GeoSurvey Report for Ethiopotash B.V, (Technical Report. ISOR-2012/028) (p. 86). Iceland Geosurvey.

Franzson, H., Helgadóttir, H. M., & Óskarsson, F. (2015). Surface exploration and first conceptual model of the Dallol geothermal area, northern Afar, Ethiopia. In *Paper Presented at Proceedings World Geothermal Congress 2015, Melbourne, Australia*.

Goldstein, R. M., Zebker, H. A., & Werner, C. L. (1988). Satellite radar interferometry: Two-dimensional phase unwrapping. *Radio Science*, *23*(4), 713–720. https://doi.org/10.1029/RS023i004p00713

Gurrola, E., Rosen, P., Sacco, G., Seliga, W., Zebker, H., Simons, M., & Sandwell, D. (2010). InSAR scientific computing environment. In *Paper Presented at American Geophysical Union Meeting, Pasadena, California.*

Hammond, J. O., Kendall, J. M., Stuart, G. W., Keir, D., Ebinger, C., Ayele, A., & Belachew, M. (2011). The nature of the crust beneath the Afar triple junction: Evidence from receiver functions. *Geochemistry, Geophysics, Geosystems*, *12*(12). https://doi.org/10.1029/2011GC003738

Hanssen, R. F. (2001). *Radar interferometry: Data interpretation and error analysis* (Vol. 2). Springer Science & Business Media.

Holwerda, J. G., & Hutchinson, R. W. (1968). Potash-bearing evaporites in the Danakil area, Ethiopia. *Economic Geology*, *63*(2), 124–150. https://doi.org/10.2113/gsecongeo.63.2.124

Illsley-Kemp, F., Keir, D., Bull, J., Gernon, T., Ebinger, C., Hammond, J. O. S., et al. (2018). Seismicity during 1036 continental breakup in the Red Sea rift of Northern Afar. *Journal of Geophysical Research: Solid Earth*, *123*(3), 2345–2362. https://doi.org/10.1002/2017JB014902

Jonsson, S., Zebker, H., Segall, P., & Amelung, F. (2002). Fault slip distribution of the 1999 Mw 7.1 Hector Mine, California, Earthquake, estimated from satellite radar and GPS measurements. *Bulletin of the Seismological Society of America*, *92*(4), 1377–1389. https://doi.org/10.1785/0120000922

Kebede, B. A., Pagli, C., Sigmundsson, F., Keir, D., La Rosa, A., & Guðbrandsson, S. (2023). Constraints on ground deformation processes at the Tulu Moye volcanic complex, Main Ethiopian Rift. *Journal of Volcanology and Geothermal Research*, *438*, 107810. https://doi.org/10.1016/j.jvolgeores.2023.107810

Keir, D., Bastow, I. D., Pagli, C., & Chambers, E. L. (2013). The development of extension and magmatism in the Red Sea rift of Afar. *Tectonophysics*, *607*, 98–114. https://doi.org/10.1016/j.tecto.2012.10.015

Kruskal, J. B. (1956). On the shortest spanning subtree of a graph and the traveling salesman problem. *Proceedings of the American Mathematical Society*, (Vol. 7, 48–50). : American Mathematical society. https://doi.org/10.2307/2033241

La Rosa, A., Pagli, C., Wang, H., Sigmundsson, F., Pinel, V., & Keir, D. (2024). Simultaneous rift-scale inflation of a deep crustal sill network in Afar, East Africa. *Nature Communications*, *15*(1), 4287. https://doi.org/10.1038/s41467-024-47136-4

Lewi, E. (2024). Seamless map of depth to the Moho interface in the Afro-Arabian region using gravity data derived from EGM2008. *Geochemistry, Geophysics, Geosystems*, *25*(7), e2023GC011322. https://doi.org/10.1029/2023GC011322

Lopez-García, J. M., Moreira, D., Benzerara, K., Grunewald, O., & López-García, P. (2020). Origin and evolution of the halo-volcanic complex of Dallol: Proto-volcanism in Northern Afar (Ethiopia). *Frontiers in Earth Science*, *7*, 351. https://doi.org/10.3389/feart.2019.00351

Makris, J., & Ginzburg, A. (1987). The Afar Depression: Transition between continental rifting and sea-floor spreading. *Tectonophysics*, *141*(1–3), 199–214. https://doi.org/10.1016/0040-1951(87)90186-7

McClusky, S., Reilinger, R., Ogubazghi, G., Amleson, A., Healeb, B., Vernant, P., et al. (2010). Kinematics of the southern Red Sea-Afar triple junction and implications for plate dynamics. *Geophysical Research Letters*, *37*(5). https://doi.org/10.1029/2009GL041127

Meaza, H., Frankl, A., Poesen, J., Zenebe, A., Deckers, J., Van Eetvelde, V., et al. (2017). Natural resource opportunities and challenges for rural development in marginal grabens-The state of the art with implications for the Rift Valley system in Ethiopia. *Journal of Arid Environments*, *147*, 1–16. https://doi.org/10.1016/j.jaridenv.2017.08.003

Moore, C., Wright, T. J., & Hooper, A. (2021). Rift Focusing and Magmatism During Late-Stage Rifting in Afar. *Journal of Geophysical Research: Solid Earth*, *126*(10), e2020JB021542. https://doi.org/10.1029/2020jb021542

Nobile, A., Pagli, C., Keir, D., Wright, T., Ayele, A., Ruch, J., & Acocella, V. (2012). Dike-fault interaction during the 2004 Dallol intrusion at the northern edge of the Erta Ale Ridge (Afar, Ethiopia). *Geophysical Research Letters*, *39*(19), L19305. https://doi.org/10.1029/2012GL053152

Okada, Y. (1985). Surface deformation due to shear and tensile faults in a half-space. *Bulletin of the Seismological Society of America*, *75*(4), 1135–1153. https://doi.org/10.1785/bssa0750041135

Otálora, F., Palero, F., Papaslioti, E. M., & García-Ruiz, J. M. (2022). Mineralochemical mechanism for the formation of salt volcanoes: The case of Mount Dallol (Afar Triangle, Ethiopia). *ACS Earth and Space Chemistry*, *6*(12), 2767–2778. https://doi.org/10.1021/acsearthspacechem.2c00075

Pagli, C., Wang, H., Wright, T. J., Calais, E., & Lewi, E. (2014). Current plate boundary deformation of the Afar rift from a 3-D velocity field inversion of InSAR and GPS. *Journal of Geophysical Research: Solid Earth*, *119*(11), 8562–8575. https://doi.org/10.1002/2014JB011391

Pagli, C., Wright, T., Ebinger, C., Yun, S., Cann, J., Barnie, T., & Ayele, A. (2012). Shallow axial magma chamber at the slow-spreading Erta Ale Ridge. *Nature Geoscience*, *5*(4), 284–288. https://doi.org/10.1038/ngeo1414

Receveur, M., Sigmundsson, F., Drouin, V., & Parks, M. (2019). Ground deformation due to steam cap processes at Reykjanes, SW-Iceland: Effects of geothermal exploitation inferred from interferometric analysis of Sentinel-1 images 2015–2017. *Geophysical Journal International*, *216*(3), 2183–2212. https://doi.org/10.1093/gji/ggy540

Rime, V., Foubert, A., Ruch, J., & Kidane, T. (2023). Tectonostratigraphic evolution and significance of the Afar Depression. *Earth-Science Reviews*, *244*, 104519. https://doi.org/10.1016/j.earscirev.2023.104519

Siebert, L., Simkin, T., & Kimberly, P. (2010). *Volcanoes of the World*. University of California Press.

Stamps, D. S., Kreemer, C., Fernandes, R., Rajaonarison, T. A., & Rambolamanana, G. (2021). Redefining east African rift system kinematics. *Geology*, *49*(2), 150–155. https://doi.org/10.1130/G47985.1

Tesfaye, S., Harding, D., & Kusky, T. (2003). Early continental breakup boundary and migration of the Afar triple 1175 junction, Ethiopia. *Geological Society of America Bulletin*, *115*(9), 1053–1067. https://doi.org/10.1130/B25149.1

UNDP. (1973). *Investigation of geothermal resources for power development, Ethiopia* (Technical Report. 860-051-01). United Nations Development Programme.

Varet, J., Chernet, T. W. G., & Arnason, K. (2012). Exploring for Geothermal Sites in Northern and Central Afar (Ethiopia). In *Paper Presented at the 4th African Rift Geothermal Conference. Nairobi, Kenya*.

Vilhjalmsson, A. M., Arnason, K., Stefansson, H. O., & Stefansson, S. A. (2012). *MT Resistivity Survey at Dallol, N-Ethiopia A Preliminary 1D Inversion* (Technical Report. ISOR-2012/027) (p. 186). Reykjavik.

Viltres, R., J´onsson, S., Alothman, A. O., Liu, S., Leroy, S., Masson, F., et al. (2022). Present-Day Motion of the Arabian Plate. *Tectonics*, *41*(3), e2021TC007013. https://doi.org/10.1029/2021TC007013

Wang, H., Elliott, J. R., Craig, T. J., Wright, T. J., Liu-Zeng, J., & Hooper, A. (2014). Normal faulting sequence in the Pumqu-Xainza Rift constrained by InSAR and teleseismic body-wave seismology. *Geochemistry, Geophysics, Geosystems*, *15*(7), 2947–2963. https://doi.org/10.1002/2014GC005369

Wang, H., Wright, T. J., & Biggs, J. (2009). Interseismic slip rate of the northwestern Xianshuihe fault from InSAR data. *Geophysical Research Letters*, *36*(3), L03302. https://doi.org/10.1029/2008GL036560

Wang, H., Wright, T. J., Yu, Y., Lin, H., Jiang, L., Li, C., & Qiu, G. (2012). InSAR reveals coastal subsidence in the Pearl River Delta, China. *Geophysical Journal International*, *191*(3), 1119–1128. https://doi.org/10.1111/j.1365-246X.2012.05687.x

Warren, J. K. (2015). *Danakhil potash, Ethiopia: Beds of kainite/carnallite, Part 2 of 4* Technical Report. SaltWork Consultants Pte Ltd. https://doi.org/10.13140/RG.2.1.2392.9769

Yang, X., Wang, H., Pagli, C., Ng, A. H. M., & He, Q. (2024). Closure-based correction of InSAR phase unwrapping errors by integrating block-wise Tikhonov regularization and flux analysis. *IEEE Transactions on Geoscience and Remote Sensing*, *62*, 1–15. https://doi.org/10.1109/TGRS.2024.3437757